

Physics-Informed Machine Learning Method for Large-Scale Data Assimilation Problems

Yu-Hong Yeung,¹ David A. Barajas-Solano,¹ Alexandre M. Tartakovsky^{2,1}

¹Physical and Computational Sciences Directorate, Pacific Northwest National Laboratory, Richland, WA 99354

²Department of Civil and Environmental Engineering, University of Illinois Urbana-Champaign, Urbana, IL 61801

Key Points:

- The modified physics-informed machine learning PICKLE method for large-scale data assimilation is proposed.
- PICKLE method is orders of magnitude faster than traditional a posteriori probability method for the considered high-resolution Hanford model.
- Trained for one set of boundary conditions, the PICKLE method can model data for different values of the boundary conditions.

arXiv:2108.00037v1 [cs.LG] 30 Jul 2021

Corresponding author: A.M. Tartakovsky, amt1998@illinois.edu

Abstract

We develop a physics-informed machine learning approach for large-scale data assimilation and parameter estimation and apply it for estimating transmissivity and hydraulic head in the two-dimensional steady-state subsurface flow model of the Hanford Site given synthetic measurements of said variables. In our approach, we extend the physics-informed conditional Karhunen-Loève expansion (PICKLE) method for modeling subsurface flow with unknown flux (Neumann) and varying head (Dirichlet) boundary conditions. We demonstrate that the PICKLE method is comparable in accuracy with the standard *maximum a posteriori* (MAP) method, but is significantly faster than MAP for large-scale problems. Both methods use a mesh to discretize the computational domain. In MAP, the parameters and states are discretized on the mesh; therefore, the size of the MAP parameter estimation problem directly depends on the mesh size. In PICKLE, the mesh is used to evaluate the residuals of the governing equation, while the parameters and states are approximated by the truncated conditional Karhunen-Loève expansions with the number of parameters controlled by the smoothness of the parameter and state fields, and not by the mesh size. For a considered example, we demonstrate that the computational cost of PICKLE increases near linearly (as $N_{FV}^{1.15}$) with the number of grid points N_{FV} , while that of MAP increases much faster as $N_{FV}^{3.28}$. We demonstrated that once trained for one set of Dirichlet boundary conditions (i.e., one river stage), the PICKLE method provides accurate estimates of the hydraulic head for any value of the Dirichlet boundary conditions (i.e., for any river stage).

1 Introduction

The ability of numerical models to predict a complex behavior of natural and engineered systems have been the main goal of computational sciences. However, when applied to natural systems such as subsurface flow and transport, predictive modeling is complicated by the inherent uncertainty in the distribution of subsurface properties, including hydraulic conductivity, that enter the subsurface models as parameters. Uniquely estimating the subsurface parameters from the measurements of parameters and states (e.g., the hydraulic head) without numerical regularization is not possible because of the ill-posedness of the arising inverse problems. To further complicate the matter, the multiple length scales of heterogeneity and time scales of flow and transport processes create enough ambiguity such that the same data can be described with different models, including deterministic and stochastic partial differential equation (PDE) models, non-local (integro-differential equation) models, and, most recently, machine learning and artificial intelligence.

In selecting the right modeling approach, one can rely on the Occam’s razor or law of parsimony principal that the simplest explanation (model) is usually the right one. However, given the abovementioned uncertainty in model parameters, the ability of models to be conditioned on spatially varying data is another critical criterion in selecting a computational model (Neuman & Tartakovsky, 2009). In theory, any model that involves observable parameters and states can be conditioned on the measurements of these variables if such are available. However, the computational cost of conditioning models on data may vary significantly.

Conditioning models on direct measurements of space-varying parameters (e.g., conductivity) is relatively straightforward and can be achieved using Kriging or Gaussian process regression (GPR) (Neuman, 1993; Tipireddy et al., 2020a). In Kriging, an estimate of the conductivity field is obtained by means of a nonlinear interpolation between its measured values with the interpolation coefficients given in terms of the covariance function of the conductivity field learned from data (Matheron, 1963; Rasmussen, 2003). Then, the flow (conditioned on the measurements of conductivity)

can be found by solving the Darcy flow equation with the conductivity field given by the Kriging estimate. The advantage of using Kriging for conditioning flow models on conductivity measurements is that it provides a Bayesian prediction, including the conditional mean (the most likely distribution of conductivity given its measurements) and the conductivity variance (a measure of uncertainty). The conditional mean and variance of conductivity can be used to obtain probabilistic estimates of the hydraulic head and fluxes conditioned on the conductivity measurements. However, conditioning deterministic or stochastic flow predictions on the measurements of both the hydraulic head and conductivity is more challenging because it requires solving an inverse problem that typically involves computing forward solutions of the Darcy equation multiple times for different realizations of the conductivity fields.

The inverse problem of computing the deterministic conductivity and hydraulic head fields given sparse measurements of these fields can be solved via *maximum a posteriori* (MAP) estimation, a Bayesian point estimation approach that consists of computing the largest mode of the posterior density of conductivity conditioned on the observations (Kitanidis, 1996; D. A. Barajas-Solano et al., 2014). A recent review of other methods for solving deterministic inverse problems can be found in A. Tartakovsky et al. (2020). Inverse uncertainty quantification problems, where the distributions of the parameters and states conditioned on the measurements are thought, are usually obtained with Bayesian methods (Herckenrath et al., 2011; Yoon et al., 2013; D. Barajas-Solano & Tartakovsky, 2019; Li & Tartakovsky, 2020).

In this work, we use the physics-informed conditional Karhunen-Loève expansion (PICKLE) method for obtaining deterministic estimates of transmissivity and head fields conditioned on the said fields measurements. We apply this method for modeling steady-state two-dimensional groundwater flow at the Hanford Site given synthetic measurements of the transmissivity and hydraulic head. The synthetic measurements are generated using the hydraulic conductivity measurements and boundary conditions obtained in the Hanford Site calibration study of Cole et al. (2001). The PICKLE method was recently introduced in A. Tartakovsky et al. (2020) for parameter estimation in PDE models for a given set of deterministically known fixed boundary conditions. Here, we extend the PICKLE method for problems with uncertain flux boundary conditions and incrementally changing Dirichlet boundary conditions. In the Hanford Site groundwater models, the latter may change in response to changing water stages in the Columbia and Yakima Rivers. The former boundary condition is used to describe recharge from the Cold Creek Valley and the Rattlesnake Springs that is difficult to estimate with a high degree of certainty. Another significant contribution of this work is testing the PICKLE methods for high-dimensional realistic conductivity fields (we find that more than 1000 terms in the KL expansion are needed to accurately approximate the log-conductivity field obtained from the Hanford Site calibration study). We compare the performance of the PICKLE and MAP methods and show that the two methods have a comparable accuracy, while the computational cost of MAP increases significantly faster with the problem size (the number elements N_{FV} in the finite volume discretization of the governing equations) than that of PICKLE, i.e., $N_{FV}^{3.28}$ in MAP versus $N_{FV}^{1.15}$ in PICKLE. In the considered examples, we observe that for $N_{FV} = 5900$, the computational time of PICKLE is one order of magnitude smaller than that of MAP. For $N_{FV} = 23600$, we estimate that PICKLE would be more than two orders of magnitude faster than MAP (the computational time of PICKLE is found to be approximately 2×10^3 s, and the computational time of MAP of approximately 5×10^5 s is estimated from the scaling relationship because it is unpractical to perform simulations for this time). The choice of synthetic (as opposite to field) measurements of the hydraulic head allows us to have the ground truth (reference) transmissivity and hydraulic head fields to compare the accuracy of the MAP and PICKLE methods, while preserving the complexity of boundary conditions and the transmissivity field of the Hanford Site.

2 Groundwater flow model and maximum a posteriori formulation of the inverse problem

We consider a two-dimensional model of groundwater flow at the Hanford Site. Our objective is to learn the spatial distribution of transmissivity $T(x): D \rightarrow \mathbb{R}^+$ and hydraulic head $u(x): D \rightarrow \mathbb{R}$ given the sparse measurements of $T(x)$ and $u(x)$, where $D \subset \mathbb{R}^2$ is the simulation domain encompassing the Hanford Site. We assume that the flow is governed by the boundary value problem (BVP)

$$\nabla \cdot [T(x)\nabla u(x)] = 0, \quad x \in D, \quad (1)$$

$$T(x)\nabla u(x) \cdot \mathbf{n}(x) = -q_{\mathcal{N}}(x), \quad x \in \Gamma_{\mathcal{N}}, \quad (2)$$

$$u(x) = u_{\mathcal{D}}(x), \quad x \in \Gamma_{\mathcal{D}}, \quad (3)$$

where $\partial D = \Gamma_{\mathcal{N}} \cup \Gamma_{\mathcal{D}}$ is the boundary of D and $\Gamma_{\mathcal{N}}$ and $\Gamma_{\mathcal{D}}$ ($\Gamma_{\mathcal{N}} \cap \Gamma_{\mathcal{D}} = \emptyset$) are the portions of the boundary where the Neumann and Dirichlet boundary conditions are prescribed, respectively. In Eq. (2), $q_{\mathcal{N}}: \Gamma_{\mathcal{N}} \rightarrow \mathbb{R}$ is the normal flux at the Neumann boundary $\Gamma_{\mathcal{N}}$, and $\mathbf{n}: \Gamma_{\mathcal{D}} \rightarrow \mathbb{R}^2$ is the unit vector normal to $\Gamma_{\mathcal{N}}$. In Eq. (3), $u_{\mathcal{D}}: \Gamma_{\mathcal{D}} \rightarrow \mathbb{R}$ is the prescribed hydraulic head on the Dirichlet boundary $\Gamma_{\mathcal{D}}$.

In this work, we assume that there are $N_{\mathbf{u}_s}$ and $N_{\mathbf{y}_s}$ observations of u and $y = \log T$, respectively, organized into the vectors \mathbf{u}_s and \mathbf{y}_s . The locations of u and y observations are organized into the arrays \mathbf{X}_u and \mathbf{X}_y , respectively. At the Hanford Site, $\Gamma_{\mathcal{D}}$ models the boundary formed by the Columbia and Yakima Rivers and $u_{\mathcal{D}}(x)$ is equal to the water levels in these rivers that are easy to measure. Therefore, $u_{\mathcal{D}}(x)$ is treated here as a known function. The homogeneous Neumann boundary condition ($q_{\mathcal{N}} = 0$) is imposed at the boundaries of formed by the (impermeable) basalt layers, and we also treat this boundary condition as known. The non-homogeneous Neumann boundary conditions are used to describe inflow/outflow of the groundwater through the boundaries formed by the Cold Creek Valley, Dry Creek Valley and Rattlesnake Spring Recharge Area. In subsurface flow models, including the Hanford Site model, (non-zero) fluxes $q_{\mathcal{N}}$ are difficult to measure directly. In this work, we consider two cases, one where $q_{\mathcal{N}}$ is known and another where $q_{\mathcal{N}}$ is unknown and is estimated along with $y(x)$ and $u(x)$.

The transmissivity field T in Eq. (1) is a differentiable function of x . Inverse problems for $T(x)$ are typically solved in the context of numerical models where Eq. (1) is discretized on a mesh and the values of T are estimated at a finite set of points on this mesh. As an example, here we consider the MAP method for estimating T values in a numerical model based on the cell-centered finite volumes (FV) discretization of Eqs. (Eq. (1))–(3) using the two-point flux approximation (TPFA) of fluxes across cell faces. In this setting, the domain D is discretized with N FV cells, and the fields u and y are discretized into values located at the cell centers $\{x_i\}_{i=1}^N$. The discrete field values are organized into the column vectors \mathbf{u} and \mathbf{y} , respectively, of a length N . The coordinates of the cell centers are organized into the array \mathbf{X}_c . In the problem formulation described below, we consider a more general case where $q_{\mathcal{N}}$ is unknown. In this case, the unknown field $q_{\mathcal{N}}(x)$ is discretized into N_q values located at the centroids of the cell faces corresponding to $\Gamma_{\mathcal{N}}$. These values are organized into the vector \mathbf{q} . After discretizing the BVP using the TPFA-FV method, we obtain the set of algebraic equations

$$\mathbf{l}(\mathbf{u}, \mathbf{y}, \mathbf{q}) = \mathbf{A}(\mathbf{y}, \mathbf{q})\mathbf{u} - \mathbf{b}(\mathbf{y}, \mathbf{q}) = 0, \quad (4)$$

with the stiffness matrix $\mathbf{A}: \mathbb{R}^N \times \mathbb{R}^{N_q} \rightarrow \mathbb{R}^{N \times N}$ and right-hand side $\mathbf{b}: \mathbb{R}^N \times \mathbb{R}^{N_q} \rightarrow \mathbb{R}^N$ defined in Appendix A. In Eq. (4), $\mathbf{l}: \mathbb{R}^N \times \mathbb{R}^N \times \mathbb{R}^{N_q} \rightarrow \mathbb{R}^N$ denotes the vector of discretized BVP residuals. The entries of the \mathbf{l} vector correspond to the FV mass balance for each of the N cells. The set of cells can be split into three sets: \mathcal{N} , the $N_{\mathcal{N}}$ cells adjacent to $\Gamma_{\mathcal{N}}$, \mathcal{D} , the $N_{\mathcal{D}}$ cells adjacent to $\Gamma_{\mathcal{D}}$, and $\mathcal{I} = [1, N] \setminus (\mathcal{D} \cup \mathcal{N})$ of cardinality $N_{\mathcal{I}} = N - N_{\mathcal{N}} - N_{\mathcal{D}}$. Only the mass balance for the cells in the \mathcal{N} set

explicitly includes the \mathbf{q} contributions; therefore, it follows that \mathbf{q} enters into \mathbf{l} only on the \mathcal{N} entries, and that $\mathbf{l}_{\mathcal{T} \cup \mathcal{D}}$ does not depend directly on \mathbf{q} .

In the MAP method, the vectors of unknown parameters \mathbf{y} and \mathbf{q} are estimated by minimizing the ℓ_2 -norm of the discrepancy between observations and model predictions, that is,

$$\begin{aligned} \min_{\mathbf{u}, \mathbf{y}, \mathbf{q}} \quad & \frac{1}{2} \|\mathbf{u}_s - \mathbf{H}_u \mathbf{u}\|_2^2 + \frac{1}{2} \|\mathbf{y}_s - \mathbf{H}_y \mathbf{y}\|_2^2 + \frac{\gamma}{2} \|\mathbf{D} \mathbf{y}\|_2^2 + \frac{\gamma}{2} \|\mathbf{q}\|_2^2, \\ \text{s.t.} \quad & \mathbf{l}(\mathbf{u}, \mathbf{y}, \mathbf{q}) = 0, \end{aligned} \quad (5)$$

where $\mathbf{H}_u: \mathbb{R}^{N_{u_s} \times N}$ and $\mathbf{H}_y: \mathbb{R}^{N_{y_s} \times N}$ are observation matrices that downsample the vectors \mathbf{u} and \mathbf{y} into the vectors of u and y values at the locations where \mathbf{u}_s and \mathbf{y}_s are measured. Specifically, $\mathbf{H}_u = \mathbf{I}_N[\mathbf{X}_u, :]$ and $\mathbf{H}_y = \mathbf{I}_N[\mathbf{X}_y, :]$ are submatrices of the identity matrix of dimension N , \mathbf{I}_N , whose rows are selected at the indices of the observation locations \mathbf{X}_u and \mathbf{X}_y , respectively. The inverse problem (5) is ill-posed; therefore, it is necessary to introduce regularization penalties to the cost function. Here, we choose to penalize the ℓ_2 -norm of the discrete gradient of the y field, and the ℓ_2 -norm of \mathbf{q} with the regularization penalty coefficient γ . In the first regularization term, $\mathbf{D}: \mathbb{R}^{N_x \times N}$ is the TPFA approximation of the gradient operator. The estimates of y and q fields obtained from Eq. (5) are equivalent to the mode of the posterior distributions of these fields in a Bayesian interpretation of the inverse problem, with the data misfit terms corresponding to a Gaussian log-likelihood, and the regularization penalties terms to a Gaussian log-prior. Here, we use MAP to benchmark the PICKLE method. The details of MAP implementation are given in Appendix B.

3 PICKLE method for inverse problems

3.1 Method formulation

The PICKLE method was proposed in A. Tartakovsky et al. (2020) for solving inverse diffusion equations with unknown diffusion coefficients. In PICKLE, the unknown parameter field $y(x)$ as well as the hydraulic head $u(x)$ are represented with the so-called conditional Karhunen-Loève expansion (CKLEs) (Tipireddy et al., 2020b) as

$$u^c(x, \boldsymbol{\eta}) = \bar{u}^c(x) + \sum_{i=1}^{N_u} \phi_i^u(x) \sqrt{\lambda_i^u} \eta_i, \quad (6)$$

$$y^c(x, \boldsymbol{\xi}) = \bar{y}^c(x) + \sum_{i=1}^{N_y} \phi_i^y(x) \sqrt{\lambda_i^y} \xi_i, \quad (7)$$

where $\boldsymbol{\eta} = (\eta_1, \eta_2, \dots)^\top$ and $\boldsymbol{\xi} = (\xi_1, \xi_2, \dots)^\top$ are the vectors of unknown CKLE coefficients, and the eigenpairs $\{\phi_i^u(x), \lambda_i^u\}_{i=1}^{N_u}$ and $\{\phi_i^y(x), \lambda_i^y\}_{i=1}^{N_y}$ are the solutions of the eigenvalue problems

$$\int_D C_u^c(x; x') \phi^u(x') dx' = \lambda^u \phi^u(x), \quad \int_D C_y^c(x; x') \phi^y(x') dx' = \lambda^y \phi^y(x). \quad (8)$$

Here, the superscript c denotes conditioning on the measurements of y . Methods for computing $\bar{y}^c(x)$, $\bar{u}^c(x)$, $C_u^c(x; x')$, and $C_y^c(x; x')$ are described in Section 3.2.

The number of KL terms N_u and N_y are selected to satisfy the following conditions:

$$\sum_{i=N_u+1}^{\infty} \lambda_i^u \leq \text{rtol}_u \int_D C_u^c(x, x) dx, \quad \sum_{i=N_y+1}^{\infty} \lambda_i^y \leq \text{rtol}_y \int_D C_y^c(x, x) dx. \quad (9)$$

For the eigenproblems solved via the eigendecomposition of the covariance matrices C_y^c and C_u^c evaluated on the cell-centered FV scheme with N cells, these conditions

can be approximated as

$$\sum_{i=N_u+1}^N \lambda_i^u \leq \text{rtol}_u \sum_{i=1}^N \lambda_i^u, \quad \sum_{i=N_y+1}^N \lambda_i^y \leq \text{rtol}_y \sum_{i=1}^N \lambda_i^y. \quad (10)$$

The inverse problem is solved by minimizing the residual $\mathbf{l}(\mathbf{u}, \mathbf{y}, \mathbf{q})$ with the substitutions of \mathbf{u} and \mathbf{y} in Eq. (4) by the CKLEs (6) and (7) evaluated at the FV cell centroids. Together with regularization penalty \mathcal{R} on $\hat{\mathbf{y}}(\boldsymbol{\xi})$ and $\hat{\mathbf{u}}(\boldsymbol{\eta})$, as well as a data misfit for u predictions, the minimization problem becomes

$$\min_{\boldsymbol{\xi}, \boldsymbol{\eta}, \mathbf{q}} \frac{1}{2} \|\mathbf{l}[\hat{\mathbf{u}}(\boldsymbol{\eta}), \hat{\mathbf{y}}(\boldsymbol{\xi}), \mathbf{q}]\|_2^2 + \frac{\beta}{2} \|\mathbf{u}_s - \mathbf{H}_u \hat{\mathbf{u}}(\boldsymbol{\eta})\|_2^2 + \frac{\alpha}{2} \mathcal{R}(\hat{\mathbf{y}}(\boldsymbol{\xi}), \hat{\mathbf{u}}(\boldsymbol{\eta})), \quad (11)$$

where $\hat{\mathbf{u}}$ and $\hat{\mathbf{y}}$ denote the PICKLE estimates of \mathbf{u} and \mathbf{y} , respectively. Here, we consider two forms of \mathcal{R} . The first form,

$$\mathcal{R} = \|\boldsymbol{\xi}\|_2^2 + \|\boldsymbol{\eta}\|_2^2, \quad (12)$$

was proposed in A. Tartakovsky et al. (2020) and shown to perform well when the reference y field is generated as a realization of a Gaussian field. We also consider a form of \mathcal{R} that penalizes the gradients of $\hat{\mathbf{u}}$ and $\hat{\mathbf{y}}$ (computed with the approximate gradient operator \mathbf{D}) as in the MAP method:

$$\mathcal{R} = \|\mathbf{D}\hat{\mathbf{y}}\|_2^2 + \|\mathbf{D}\hat{\mathbf{u}}\|_2^2. \quad (13)$$

The PICKLE formulation (11) is different from that of A. Tartakovsky et al. (2020) because it allows for unknown flux boundary conditions. Below, we propose a cost-effective treatment of this problem. As noted in Section 2, the FV mass balances for the subset $\mathcal{I} \cup \mathcal{D}$ of cells (which includes the vast majority of cells) do not directly involve the vector of normal fluxes \mathbf{q} . This allows us to exclude \mathbf{q} from the inverse problem by penalizing the ℓ_2 -norm of $\mathbf{l}_{\mathcal{I} \cup \mathcal{D}}$, i.e., to only minimize residuals within \mathcal{I} and \mathcal{D} cells:

$$\min_{\boldsymbol{\xi}, \boldsymbol{\eta}} \frac{1}{2} \|\mathbf{l}_{\mathcal{I} \cup \mathcal{D}}[\hat{\mathbf{u}}(\boldsymbol{\eta}), \hat{\mathbf{y}}(\boldsymbol{\xi})]\|_2^2 + \frac{\beta}{2} \|\mathbf{u}_s - \mathbf{H}_u \hat{\mathbf{u}}(\boldsymbol{\eta})\|_2^2 + \frac{\alpha}{2} \mathcal{R}(\hat{\mathbf{y}}(\boldsymbol{\xi}), \hat{\mathbf{u}}(\boldsymbol{\eta})). \quad (14)$$

A PICKLE estimate of \mathbf{q} is then obtained by solving

$$\mathbf{l}_{\mathcal{N}}[\hat{\mathbf{u}}(\hat{\boldsymbol{\eta}}), \hat{\mathbf{y}}(\hat{\boldsymbol{\xi}}), \hat{\mathbf{q}}] = 0, \quad (15)$$

where $\hat{\boldsymbol{\xi}}$ and $\hat{\boldsymbol{\eta}}$ are the solutions of the minimization problem (14). We note that $\mathbf{l}_{\mathcal{N}}$ is linear in \mathbf{q} , so that the solution of Eq. (15) is trivial.

Because we use a CKLE model $\hat{\mathbf{y}}(\boldsymbol{\xi})$ for \mathbf{y} , it satisfies the y observations by construction. The u field is approximated with the KLE model $\hat{\mathbf{u}}(\boldsymbol{\eta})$ that is not conditioned on the u measurements. Therefore, we have included a data misfit term with coefficient β in Eq (14) penalizing the deviation between u predictions and observations.

We use the Trust Region Reflective algorithm (Branch et al., 1999) to solve minimization problems in both PICKLE and MAP methods. To do this, we cast both Eqs. (5) and (14) as least-squares problems. The least-squares minimization algorithm requires the evaluations of the Jacobian matrix \mathbf{J} of the objective vector, which is also the most computationally demanding part of the least-squares minimization. Jacobian evaluation in the PICKLE method only requires computing the derivatives of the PDE residuals with respect to the CKLE coefficients. This is in general significantly less expensive than solving the BVP and the corresponding adjoint problem in the MAP's

Jacobian evaluation procedure (D. A. Barajas-Solano et al., 2014). In addition, the cost of Jacobian evaluation depends on the Jacobian matrix size, which is $(N_{\mathcal{I}} + N_{u_s} + N_{u_y}) \times N$ in MAP (N is the number of the FV cells) and $(N + N_{u_s} + N_u + N_y) \times (N_u + N_y)$ in PICKLE. Depending on the field smoothness and the required resolution, N_u and N_y can be much smaller than N . The details of the optimization algorithm are given in Appendix C.

3.2 Computing covariance functions

To construct $C_y^c(x, y)$, we first estimate the unconditional covariance of y , $C_y(x, y)$ by assuming it has the 5/2-Matérn kernel

$$C_y(x, y) = \sigma^2 \left(1 + \sqrt{5} \frac{|x - y|}{\lambda} + \frac{5}{3} \frac{|x - y|^2}{l^2} \right) \exp \left(-\sqrt{5} \frac{|x - y|}{l} \right),$$

where σ and l are the standard deviation and the correlation length of y that are estimated from \mathbf{y}_s by minimizing the marginal log-likelihood function (Rasmussen, 2003). The conditional mean and covariance of y are then computed from the GPR (or Kriging) equations

$$\bar{y}^c(x) = \mathbf{C}(x) \mathbf{C}_s^{-1} \mathbf{y}_s, \quad (16)$$

$$C_y^c(x, x') = C_y(x, x') - \mathbf{C}(x) \mathbf{C}_s^{-1} \mathbf{C}(x'), \quad (17)$$

where \mathbf{C}_s is the $N_{\mathbf{y}_s} \times N_{\mathbf{y}_s}$ observation covariance matrix with elements $C_{s,ij} = C_y(x_i, x_j)$ and $\mathbf{C}(x)$ is the $N_{\mathbf{y}_s}$ -dimensional vector with the components $C_i(x) = C_y(x, x_i)$, where $x_i, x_j \in \mathbf{X}_y$. The evaluation of \bar{u}^c and $C_u^c(x, x')$ from u measurements using the marginal likelihood maximization is not adequate for two related reasons: (1) the $u(x)$ field is not stationary (i.e., the covariance kernel of u depends on x and y and not just the distance between x and y as in, e.g., the Matérn kernel), and guessing a nonstationary covariance kernel for u and then training it could be very challenging; and (2) this purely data-driven approach does not enforce the governing equations and boundary conditions on the mean and covariance function even approximately. Therefore, in this work we employ a Monte Carlo (MC) simulation-based method for computing the conditional mean and covariance of u .

In the MC method, we treat the partially known $u(x)$ and $y(x)$ as random variables $\tilde{u}^c(x, \omega)$ and $\tilde{y}^c(x, \omega)$, $\{\tilde{u}^c, \tilde{y}^c\} : D \times \Omega \rightarrow \mathbb{R}$ (where Ω is the corresponding random outcome space) conditioned on observed measurements of y . We model $\tilde{y}^c(x, \omega)$ using the *stochastic* truncated CKLEs

$$\tilde{y}^c(x, \tilde{\boldsymbol{\xi}}(\omega)) = \bar{y}^c(x) + \sum_{i=1}^{N'_y} \phi_i^y(x) \sqrt{\lambda_i^y} \tilde{\xi}_i(\omega), \quad (18)$$

where $\tilde{\boldsymbol{\xi}}(\omega) = (\tilde{\xi}_1(\omega); \tilde{\xi}_2(\omega); \dots)^\top$ is the vectors of independent and identically distributed Gaussian random variables. The eigenpairs $\{\phi_i^y(x); \lambda_i^y\}_{i=1}^{N'_y}$ satisfy the same eigenvalue problem (8) as those in the deterministic CKLE of Eq. (7). We note that, N'_y does not need to be the same as N_y in Eq. (6), e.g., it can be chosen with smaller *rtol_y* to obtain a more accurate MC solution. However, in this study we set $N'_y = N_y$. Next, we construct an ensemble of N_{ens} realizations of \tilde{y}^c , $\{y^{c,(i)}\}_{i=1}^{N_{\text{ens}}}$ by sampling $\boldsymbol{\xi}^{(i)}$ from $\mathcal{N}(0, \mathbf{I}_{N'_y})$ and evaluating the CKLE model (18) with $\tilde{\boldsymbol{\xi}} = \boldsymbol{\xi}^{(i)}$.

The Dirichlet and Neumann boundaries $\Gamma_{\mathcal{D}}$ and $\Gamma_{\mathcal{N}}$ are defined in the Hanford Site calibration study and are shown in Figure 2. This calibration study also provides the estimates of the head $u_{\mathcal{D}}(x)$ and fluxes $q_{\mathcal{N}}$ at these boundaries. In this work we assume that $u_{\mathcal{D}}(x)$ is known (in Sections 4.2 and 4.3, $u_{\mathcal{D}}(x)$ is given by the aforementioned calibration study, and in Section 4.5, $u_{\mathcal{D}}(x)$ is modified from the calibrated values to simulate the changing water levels in the Columbia and Yakima Rivers).

In cases with unknown $q_{\mathcal{N}}$, we assume that $q_{\mathcal{N}}$ is a Gaussian random field with the known mean and variance that we compute from the $q_{\mathcal{N}}$ values in the aforementioned calibration study.

Next, we generate N_{ens} random realizations of $q_{\mathcal{N}}(x)$, $\{q_{\mathcal{N}}^{(i)}(x)\}_{i=1}^{N_{\text{ens}}}$. For each member of the ensemble $y^{c,(i)}$ and the corresponding Neumann boundary condition $q_{\mathcal{N}}^{(i)}(x)$, we calculate $u^{(i)}$ by solving the PDE problem (1)–(3). The resulting ensemble $\{u^{(i)}\}_{i=1}^{N_{\text{ens}}}$ is used to compute the N -dimensional vector of mean values of u in each FV cell,

$$\bar{u}^c(x_j) = \frac{1}{N_{\text{ens}}} \sum_{i=1}^{N_{\text{ens}}} u^{(i)}(x_j), \quad x_j \in \mathbf{X}_c, \quad (19)$$

and the $N \times N$ covariance matrix of u with elements

$$C_u^c(x_p, x_q) = \frac{1}{N_{\text{ens}} - 1} \sum_{i=1}^{N_{\text{ens}}} \left[u^{(i)}(x_p) - \bar{u}(x_p) \right] \left[u^{(i)}(x_q) - \bar{u}(x_q) \right], \quad (x_p, x_q) \in \mathbf{X}_c. \quad (20)$$

In this work, we set N_{ens} large enough to assure that the PICKLE estimates of y do not change with further increase of N_{ens} . In general, for $C_u^c(x_p, x_q)$ to have at least N_u non-zero eigenvalues λ_i^u , the ensemble size should be $N_{\text{ens}} > N_{\mathbf{u}_s}$. When it is not feasible to perform $N_{\text{ens}} > N_{\mathbf{u}_s}$ MC simulations, shrinkage estimators can be employed to regularize the covariance matrix estimation (Chen et al., 2009). The accuracy of the covariance estimation with a small number of MC simulations can be increased by performing additional less-expensive coarser-resolution simulations using the Multilevel MC approach (Giles, 2015; X. Yang, Tartakovsky, & Tartakovsky, 2018; X. Yang et al., 2019). Also, there are several computationally efficient alternatives to MC methods, including the moment equation method (e.g., (Neuman, 1993; D. M. Tartakovsky et al., 2003; Jarman & Tartakovsky, 2013)) and polynomial-chaos-based approaches (Lin & Tartakovsky, 2010; Tipireddy et al., 2020a; Li & Tartakovsky, 2020), surrogate models (X. Yang, Li, & Tartakovsky, 2018), and generative physics-informed machine learning methods (L. Yang et al., 2019).

4 Numerical Experiments

4.1 Synthetic data sets

We compare the performance of the PICKLE and MAP methods for parameter and state estimation in the steady-state two-dimensional groundwater model of the Hanford Site. In this comparison study, we use two reference transmissivity fields $y(x) = \ln T(x)$ and boundary conditions $u_{\mathcal{D}}(x)$ and $q_{\mathcal{N}}(x)$ that are based on the three-dimensional Hanford Site calibration study (Cole et al., 2001). This calibration study was performed on the unstructured quadrilateral grid shown in Figure 1a with 4 to 17 horizontal layers depending on the Cartesian plane coordinates and produced an estimate of the three-dimensional conductivity field. We obtain the first reference transmissivity field by depth averaging the conductivity field over the unstructured mesh.

The original lateral mesh contains three different mesh resolutions and includes both the western and eastern banks of the Columbia River (the ‘‘Columbia River’’ cells are highlighted in blue in Figure 1a). We simplify the mesh by removing the river cells and prescribing Dirichlet BC on the western side of the Columbia River and by coarsening the mesh to achieve a uniform resolution, as shown in Figure 1b. For mesh coarsening, we use a semi-automatic algorithm to merge groups of finer cells into a single cell while maintaining that the mesh is boundary-conforming and each cell is a quadrilateral. The resulting mesh has 1475 cells. The transmissivity of each coarse cell is computed as the geometric average of the transmissivities of the replaced finer

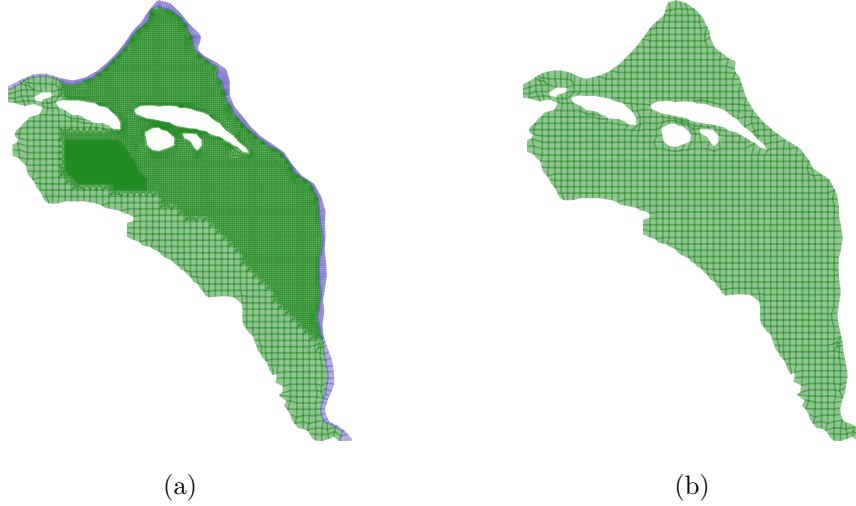


Figure 1: (??) Mesh of the Hanford site subsurface flow model in the calibration study of Cole et al. (2001). Cells that represent Columbia River are highlighted in blue with the river head boundary conditions prescribed at the vertices of these cells. (??) A quasi-uniform coarse mesh with the $N_{FV} = 1475$ cells used in this study.

cells. The transmissivity field corresponding to the coarse mesh is shown in Figure 2. We refer to this field as *reference field 1* (“RF1”). We note that the PICKLE method can employ the FV (as in this study) or finite elements discretization to evaluate the residuals and, therefore, can utilize a multiresolution mesh.

Figure 2 also shows the locations of some of the wells at the Hanford Site. We note that the calibration study (Cole et al., 2001) gives coordinates of 558 wells at the Hanford Site but that some of these wells are located in the same coarse or fine cells. Because our model uses exclusively cells and not points to denote spatial locations, multiple wells are considered as one measurement if they are located in the same cell. As a result, there are 323 in the FV model shown in Figure 2.

We hypothesize that the accuracy of the PICKLE method depends on the smoothness of the reference transmissivity field. To test this hypothesis, we generate the *reference field 2* (“RF2”) transmissivity field in addition to RF1 field using GPR (Eq. (16)) and 50 measurements drawn from the RF1 field at the locations randomly picked from the locations of the wells. By construction, the RF2 field is smoother than the RF1 field.

We also study the performance of PICKLE relative to MAP as a function of the size of the FV model resolution. For this, we generate a higher-resolution mesh by splitting each cell in the mesh in Figure 1b ($1\times$ resolution) into four ($4\times$ resolution) equiareal cells, resulting in 5,900 cells. We note that there are 408 wells at this resolution.

For each reference transmissivity field $y_{ref}(x) = \ln T_{ref}(x)$, we generate the hydraulic head field $u_{ref}(x)$ by solving the Darcy flow equation on the corresponding mesh with the deterministic Dirichlet and Neumann boundary conditions from the calibration study (Cole et al., 2001). Then, we randomly pick $N_{\mathbf{y}_s}$ well locations and treat the values of y_{ref} at these locations as y measurements. Similarly, we draw $N_{\mathbf{u}_s}$ measurements of the hydraulic head u from $u_{ref}(x)$. These measurements are treated

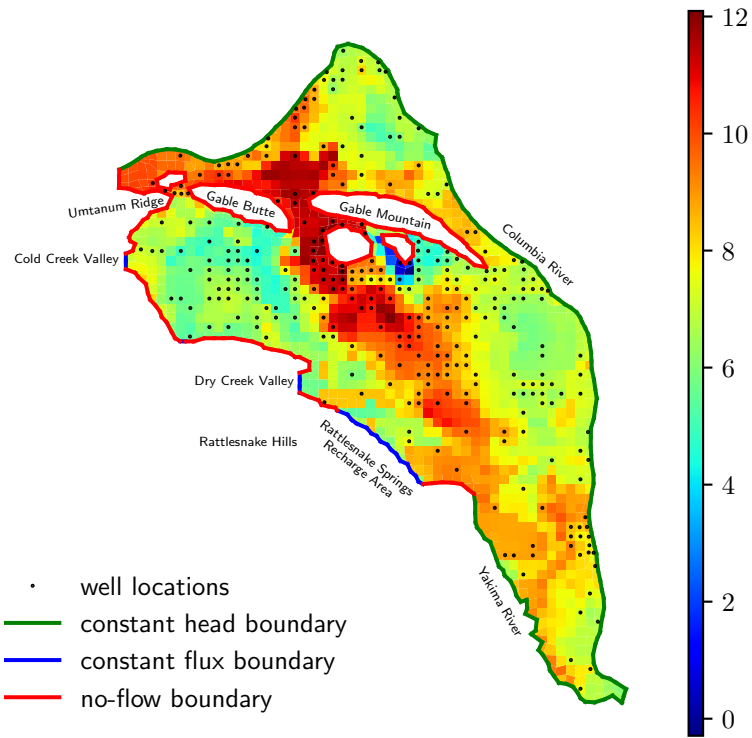


Figure 2: The coarse-resolution ($N_{FV} = 1475$) RF1 y field, well locations, and the parts of boundaries where different types of boundary conditions are prescribed.

as synthetic data sets and used in the PICKLE and MAP methods to estimate the $y(x)$ and $u(x)$ fields.

All PICKLE and MAP simulations are performed using a 3.2 GHz 8-core Intel Xeon W CPU and 32 GB of 2666 MHz DDR4 RAM. Codes are written in Python using the NumPy and SciPy packages.

The weights in the PICKLE and MAP minimization problems are empirically found to minimize the error with respect to the reference y fields as $\beta = 10$, $\alpha = 10^{-4}$, and $\gamma = 10^{-4}$. When a reference field is not known, these weights could be found using the standard cross-validation methods (Picard & Cook, 1984).

4.2 RF1 reference field

First, we use PICKLE to estimate y and u on the coarse mesh with 1475 cells with the measurements of y and u drawn from the synthetic set generated with the RF1 reference field. We start with the unknown Neumann boundary condition case. The number of terms in the KL expansions of y and u are set to $N_y = 1000$ and $N_u = 1000$, respectively. The corresponding relative tolerances are for these choices of N_y and N_u are $\text{rtol}_u = \sum_{i=N_u+1}^N \lambda_i^u / \sum_{i=1}^N \lambda_i^u = 6.4 \times 10^{-6}$ and $\text{rtol}_y = \sum_{i=N_y+1}^N \lambda_i^y / \sum_{i=1}^N \lambda_i^y = 2.8 \times 10^{-8}$, respectively. We assume that u measurements are available at all wells, i.e., $N_{\mathbf{u}_s} = 323$. For the RF1 field, we find that Eq. (13) regularization in the PICKLE method provides more accurate results than Eq. (12) regularization. For example, for 10 different spatial distributions of 50 observations of y , the relative l_2 errors in the estimated y field are in the ranges of 0.39-0.88 and 0.41-1.06 for regularizers given by Eqs. (13) and (12), respectively. The relative l_2 errors are computed on the FV mesh as

$$\varepsilon_y = \frac{\|\hat{\mathbf{y}} - \mathbf{y}_{ref}\|_2}{\|\mathbf{y}_{ref}\|_2}.$$

Therefore, in all cases considered in this section we are using the Eq. (13) regularization.

Figure 3 shows the distribution of point errors in the PICKLE and MAP estimates of y relative to the RF1 y field obtained with $N_{\mathbf{y}_s} = 25, 50, 100,$ and 200 y observations. For the considered measurement locations, the PICKLE and MAP methods have comparable accuracy for $N_{\mathbf{y}_s} \geq 50$, with MAP being more accurate for $N_{\mathbf{y}_s} = 25$.

Because the inverse problem for y is ill-posed, the regularized PICKLE and MAP solutions depend not only on the number of measurements but also on the measurement locations. To study the effect of the measurement locations on the PICKLE and MAP estimation errors, for each value $N_{\mathbf{y}_s}$, we randomly generate 10 distributions of y measurement locations and estimate y for each of these locations distributions. Table 1a shows the ranges of relative l_2 and absolute l_∞ errors in the PICKLE and MAP y estimates as well as the number of iterations in the minimization algorithm and the execution time (in seconds) for $N_{\mathbf{y}_s}$ ranging from 25 to 400. For comparison, we also show errors in y estimated with the GPR Eq (16). The l_∞ error is defined as the maximum of $|\hat{y}(x_i) - y_{ref}(x_i)|$ ($i = 1, \dots, N$), where $\hat{y}(x_i)$ and $y_{ref}(x_i)$ are the values of the estimated and reference y fields at the center of the i th FV cell, respectively.

As expected, the accuracy of all methods increases with $N_{\mathbf{y}_s}$. The PICKLE method is on average slightly less accurate than MAP in terms of both l_2 and l_∞ errors. However, MAP is more sensitive to the measurements locations. For example, for $N_{\mathbf{y}_s} = 100$ and 200 , we observe that in MAP the maximum l_2 errors are 2.43 and 1.25, respectively, versus 0.5 and 0.38 in PICKLE. We attribute the higher robustness of PICKLE relative to MAP with respect to measurement locations to the regularization

effect of the CKLE representation of y . We also note that GPR has significantly larger errors than those in PICKLE and MAP for all considered examples.

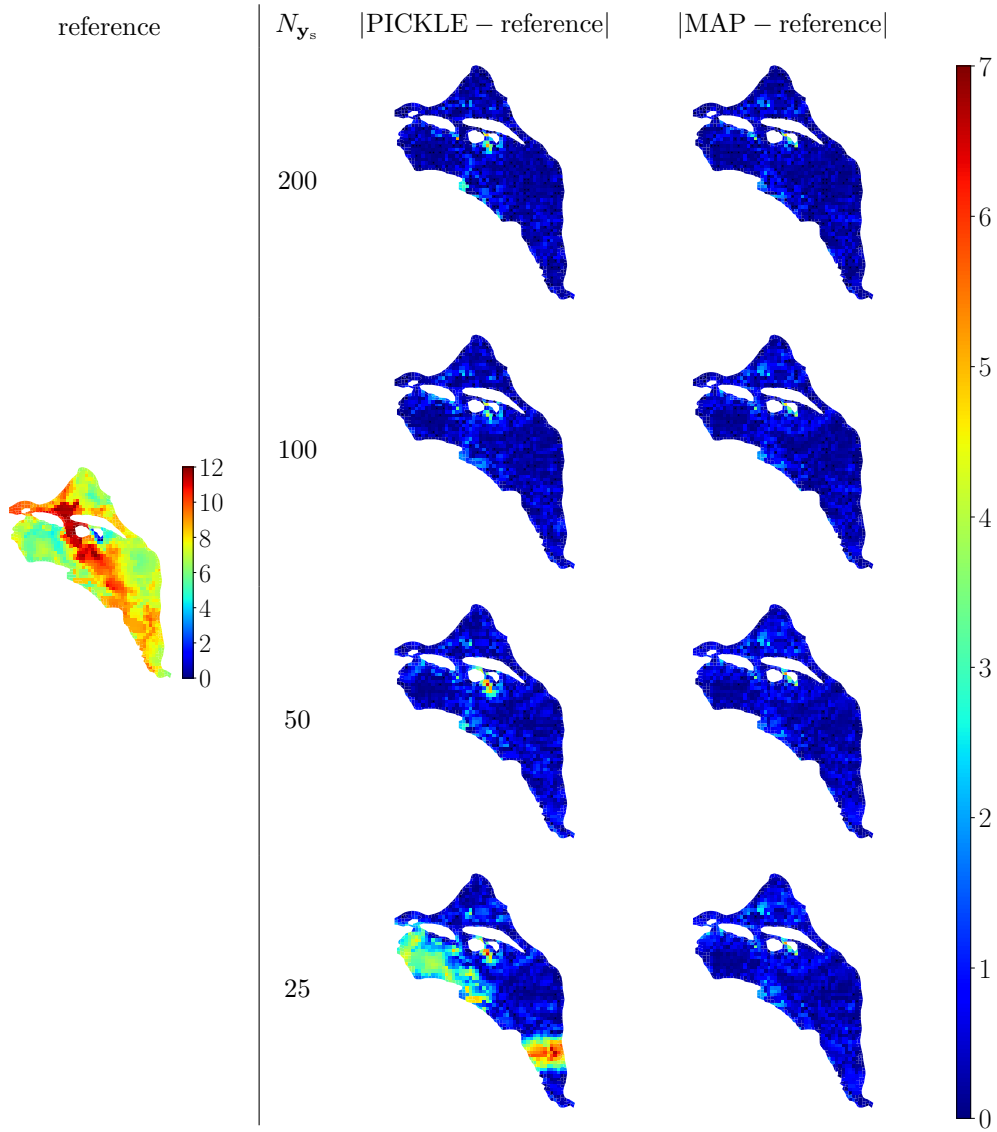


Figure 3: The coarse-resolution ($N_{FV} = 1475$) RF1 reference y field and the point errors in the PICKLE and MAP estimates of the y field as functions of N_{y_s} given the unknown Neumann boundary conditions. The dots are the locations of the 100 observations of y .

Table 1a also shows that the computational cost of PICKLE is significantly smaller than the cost of MAP, and the cost difference increases with increasing N_{y_s} . Note that we give the total execution time of PICKLE that includes the cost of MC evaluation of the mean and covariance of u (approximately 28 s), GPR (approximately 0.4 s), and eigendecomposition (approximately 2.9 s). The computational cost of GPR for the considered problem is negligible relative to both PICKLE and MAP, and we do not show it in this table. As with the estimation errors, we observe that the computational cost of PICKLE is significantly less sensitive to the measurement locations than that of MAP. For example, the ratio between the PICKLE maximum and minimum execution times in 10 realizations for $N_{y_s} = 25$ and 400 are 2.74 and 2.64, respec-

tively. In MAP, for the same values of $N_{\mathbf{y}_s}$, these ratios are 4.01 and 16.51. The larger variability in the MAP computational time corresponds to the larger variability in the number of iterations in the MAP's least-square minimization algorithm.

Table 1: Performance of PICKLE and MAP in estimating the coarse-resolution ($N_{FV} = 1475$) RF1 as functions of $N_{\mathbf{y}_s}$ with (a) unknown and (b) known Neumann boundary conditions.

(a) Unknown Neumann boundary conditions

		$N_{\mathbf{y}_s}$				
solver		400	200	100	50	25
least square iterations	PICKLE	12–35	13–23	14–30	17–64	18–51
	MAP	25–400	27–603	22–535	33–483	93–357
execution time (s)	PICKLE	143.26–378.35	144.73–253.47	142.71–300.60	159.94–592.47	180.43–495.34
	MAP	116.74–1928.08	121.87–2737.72	70.40–2283.90	126.52–2134.91	402.08–1613.52
relative ℓ_2 error	GPR	0.29–0.35	0.40–0.48	0.50–0.66	0.62–0.76	0.74–1.03
	PICKLE	0.24–0.29	0.32–0.38	0.35–0.50	0.42–0.64	0.55–1.20
	MAP	0.22–0.26	0.28–1.25	0.32–2.43	0.36–0.42	0.40–0.55
absolute ℓ_∞ error	GPR	3.74–5.87	3.79–7.39	4.24–8.00	5.64–8.27	6.21–9.71
	PICKLE	3.68–5.16	4.17–6.57	4.36–6.10	4.52–6.40	4.61–7.57
	MAP	3.68–6.30	3.72–39.49	4.06–79.01	4.07–6.51	3.91–6.29

(b) Known Neumann boundary conditions

		$N_{\mathbf{y}_s}$				
solver		400	200	100	50	25
least square iterations	PICKLE	28–54	29–55	37–85	31–78	47–158
	MAP	1081–2626	1488–4143	3497–19048	5343–13247	7662–15694
execution time (s)	PICKLE	119.43–216.47	119.43–216.47	137.37–324.25	120.67–305.00	155.06–510.83
	MAP	232.30–545.90	320.33–836.32	726.96–3649.97	1072.23–2582.03	1544.52–3133.03
relative ℓ_2 error	PICKLE	0.24–0.27	0.30–0.35	0.34–0.46	0.39–0.88	0.44–1.47
	MAP	0.21–0.29	0.27–0.30	0.31–0.36	0.35–0.42	0.39–0.45
absolute ℓ_∞ error	PICKLE	3.48–4.99	3.62–5.43	4.32–5.45	4.87–8.76	4.55–9.51
	MAP	3.15–5.55	3.65–6.45	3.64–6.40	4.91–6.39	5.37–6.57

Next, we investigate the performance of the PICKLE and MAP methods as functions of $N_{\mathbf{y}_s}$ when the Neumann boundary conditions are known. We note that the GPR method for estimating y is based solely on y measurements and, therefore, is

independent of the boundary conditions. Therefore, we do not present GPR errors in this comparison study. Table 1b shows the errors and execution time in the PICKLE and MAP methods for the same sets of y measurements as in the unknown Neumann boundary condition cases. We find that the errors of both methods only slightly decrease (less than 5%) relative to the unknown Neumann boundary condition cases. The execution time of PICKLE is practically not affected by whether the Neumann boundary conditions are known deterministically or stochastically, while the MAP execution time is increased.

Theoretically, increasing the number of KL terms in the CKLE of y should increase the accuracy of PICKLE because it allows capturing more accurately the spatial correlation structure of $y(x)$. However, increasing the number of KL terms also increases the number of unknown parameters and, therefore, the computational cost of PICKLE. In Tables 2a and 2b, we compare the errors and execution time of PICKLE with 1000 and 1400 terms in the y CKLE for the cases with unknown and known boundary conditions, respectively. We observe that increasing the number of KL terms does not lead to a significant increase in the accuracy of PICKLE. The ℓ_2 error decreases slightly, with only significant (10%) improvement for the smallest considered number ($N_{\mathbf{y}_s} = 50$) of y measurements. This is because $N_y = 1000$ already corresponds to a very small value of $\text{rtol}_y = 2.8 \times 10^{-8}$. The further increase in N_y does not significantly improve the approximation power of the CKLE, but makes the minimization problem computationally more difficult and costly. We observe a slight increase in the ℓ_∞ errors due to the fact that the larger number of KL terms might require a stronger regularization (i.e., larger values of β). On the other hand, the increase in N_y leads to a significant increase in the execution time of PICKLE, by approximately a factor of 4 for $N_{\mathbf{y}_s} = 50$ and a factor of 2 for $N_{\mathbf{y}_s} = 100, 200$, and 323.

4.3 RF2 reference field

Here, we estimate y and u using the synthetic measurements of y and u generated on the coarse and fine meshes for the RF2 reference field. We assume that u measurements are available at all wells, i.e., $N_{\mathbf{u}_s} = 323$ and 408 on the coarse and fine meshes, respectively. As in Section 4.2, the number of KL terms in the y and u expansions is set to $N_y = N_u = 1000$. The corresponding relative tolerances for these choices of N_y and N_u are $\text{rtol}_u = 3.01 \times 10^{-9}$ and $\text{rtol}_y = 7.9 \times 10^{-6}$, respectively. Opposite to our results for the RF1 field, here we find that the Eq. (12) regularization in the PICKLE method provides more accurate results than the Eq. (13) regularization. For 10 different spatial distributions of 50 observations of y , the relative ℓ_2 errors in the estimated y field are in the ranges of 0.21–0.40 and 0.0423–0.145 for regularizers given by Eqs. (13) and (12), respectively. Therefore, in this section we are using the Eq. (12) regularization.

Figure 4 shows the RF2 reference y field and the point errors in the PICKLE and MAP estimates of the y field on the coarse mesh obtained with $N_{\mathbf{y}_s} = 10, 25, 50$, and 100 for the unknown Neumann boundary conditions. The locations of y measurements are randomly selected from the well locations. Table 3 lists the ranges of ℓ_2 and ℓ_∞ errors in the y estimates as functions of $N_{\mathbf{y}_s}$ obtained with the PICKLE, GPR, and MAP methods. For each $N_{\mathbf{y}_s}$, 10 different random configurations of the measurement locations are selected to compute the ranges. Subtables (a) and (b) give results for unknown and known Neumann boundary conditions, respectively. PICKLE's ℓ_2 errors are smaller than those in MAP for $N_{\mathbf{y}_s} = 50$ and 100. For $N_{\mathbf{y}_s} = 10$ and 25, the lower bounds of ℓ_2 errors are smaller in PICKLE and the upper bounds are smaller in MAP. The absolute ℓ_∞ errors follow the same pattern as the ℓ_2 errors.

For this coarse resolution, the execution time of PICKLE is larger than that of MAP. Both PICKLE and MAP perform well for unknown Neumann boundary

Table 2: Performance of PICKLE as a function of the number of KL terms for estimating the coarse-resolution RF1 field with (a) unknown and (b) known Neumann boundary conditions.

(a) Unknown Neumann boundary conditions

	KL terms	$N_{\mathbf{y}_s}$			
		323	200	100	50
least square iterations	1000	9	13	19	36
	1400	9	10	15	67
execution time (s)	1000	81.59	115.46	166.63	317.18
	1400	179.37	202.58	306.18	1374.94
relative ℓ_2 error	1000	0.32	0.39	0.44	0.58
	1400	0.32	0.37	0.42	0.48
absolute ℓ_∞ error	1000	5.20	5.36	5.07	6.49
	1400	5.32	5.50	5.49	6.57

(b) Known Neumann boundary conditions

	KL terms	$N_{\mathbf{y}_s}$			
		323	200	100	50
least square iterations	1000	9	13	18	23
	1400	9	11	12	42
execution time (s)	1000	80.88	116.97	169.18	199.28
	1400	179.82	226.61	238.54	887.05
relative ℓ_2 error	1000	0.31	0.38	0.43	0.56
	1400	0.31	0.37	0.43	0.49
absolute ℓ_∞ error	1000	5.37	5.38	5.14	6.43
	1400	5.39	5.42	5.51	6.51

Table 3: Performance of PICKLE and MAP for estimating the coarse-resolution ($N_{FV} = 1475$) RF2 as functions of N_{y_s} with (a) unknown and (b) known Neumann boundary conditions.

(a) Unknown Neumann boundary conditions

		N_{y_s}			
solvers		100	50	25	10
least square iterations	PICKLE	9–11	11–14	11–18	15–47
	MAP	14–144	14–62	14–87	16–346
execution time (s)	PICKLE	83.4–114	81.5–105	85.3–138	56.7–136
	MAP	38.1–306	29.5–138	28.4–191	19.2–310
relative ℓ_2 error	GPR	0.118–0.175	0.207–0.398	0.353–0.513	0.468–0.875
	PICKLE	0.0300–0.0450	0.0539–0.145	0.0876–0.232	0.174–0.816
	MAP	0.0892–0.107	0.109–0.163	0.150–0.227	0.198–0.300
absolute ℓ_∞ error	GPR	1.04–2.37	2.11–4.36	2.05–4.29	3.34–4.45
	PICKLE	0.781–0.854	0.792–1.20	0.831–1.51	1.18–3.61
	MAP	0.790–1.09	0.858–1.49	1.08–1.44	1.09–1.49

(b) Known Neumann boundary conditions

		N_{y_s}			
solvers		100	50	25	10
least square iterations	PICKLE	9–11	11–14	11–17	14–30
	MAP	14–47	14–53	17–193	61–109
execution time (s)	PICKLE	72.8–94	53.5–68.2	53.3–71.8	58.2–107
	MAP	39.5–326	66.4–121	72.1–122	66.6–126
relative ℓ_2 error	PICKLE	0.0291–0.0411	0.0423–0.145	0.0773–0.245	0.129–0.547
	MAP	0.0857–0.102	0.103–0.156	0.155–0.251	0.174–0.280
absolute ℓ_∞ error	PICKLE	0.734–0.985	0.794–1.28	0.834–1.46	1.06–2.45
	MAP	0.800–1.08	0.873–1.47	1.02–1.45	1.02–1.49

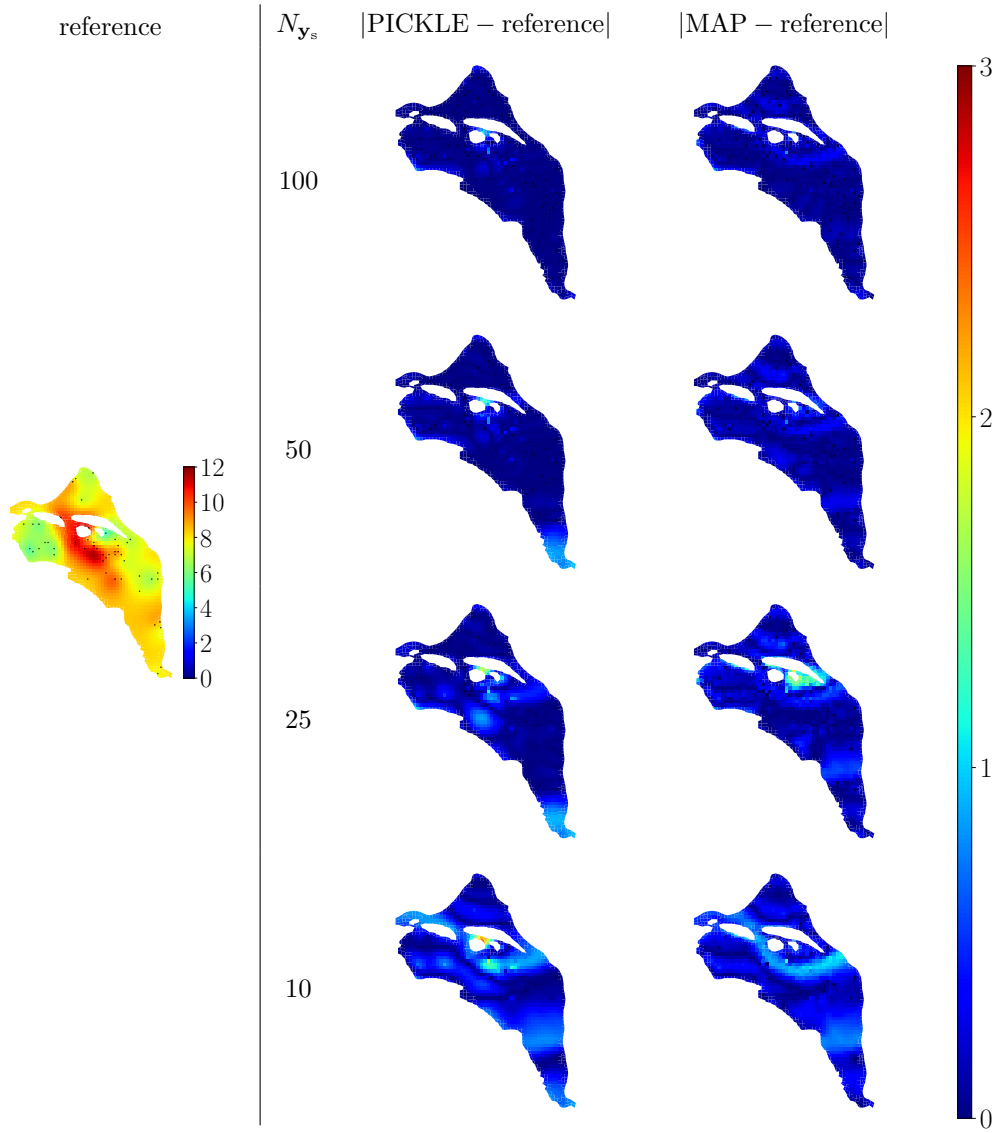


Figure 4: The coarse-resolution ($N_{FV} = 1475$) RF2 reference y field and the point errors in the PICKLE and MAP estimates of the y field as functions of N_{y_s} given the unknown Neumann boundary conditions. The dots are the locations of the 100 observations of y .

conditions with estimation errors being only slightly larger than those in the case with known Neumann boundary conditions. The ℓ_2 and ℓ_∞ errors in estimating the RF2 field are significantly smaller than those in estimating the RF1 field, which is not surprising given the relative smoothness of the RF2 field. For the same reason, the execution time of both PICKLE and MAP methods is significantly smaller for modeling measurements from RF2 than RF1.

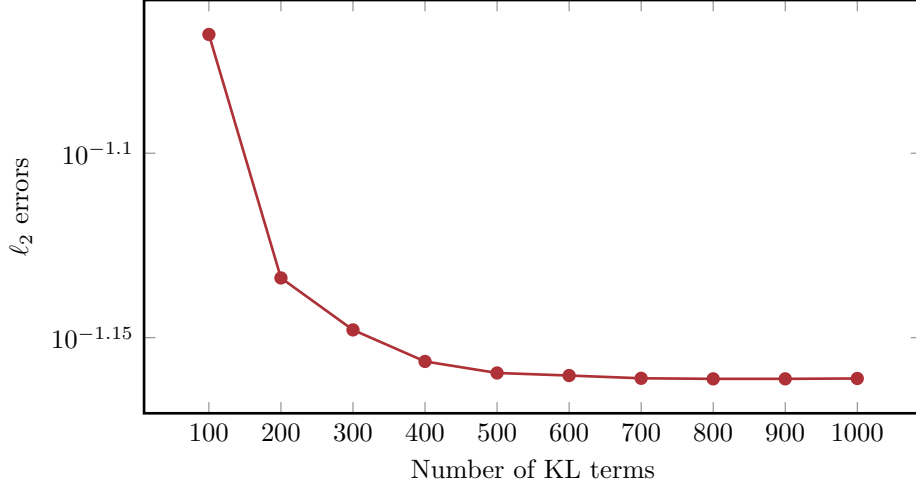


Figure 5: Relative ℓ_2 errors versus the number of KL terms.

Next, we study the relative ℓ_2 error in the PICKLE solution for $y(x)$ as a function of N_y and N_u , the number of terms in the CKLE of y and u , respectively, for $N_{\mathbf{y}_s} = 100$. For simplicity, we set $N_y = N_u$. Figure 5 shows that error decreases as N_y increases and, for the considered RF2 field, reaches the asymptotic value of less than 0.07 at $N_y \approx 800$. Therefore, the rtol_y on the order of 10^{-6} , which is used in this, and the corresponding $N_y = 1000$ are sufficient to obtain an accurate approximating of the RF2 y field and the corresponding reference u field. We note that for the (diffusion-type) Darcy equation, the solution $u(x)$ is always smoother than the parameter field $y(x)$. Therefore, the computational cost of PICKLE can be reduced by setting $\text{rtol}_u = \text{rtol}_y$, which for diffusion equations would result in $N_u < N_y$.

Finally, we test the relative performance of the PINN and MAP methods as a function of the resolution of the flow model by estimating y and u using the finer mesh with $N_{VF} = 5900$. Table 4 lists the ranges of ℓ_2 and ℓ_∞ errors in the PICKLE, GPR, and MAP estimates of y as functions of $N_{\mathbf{y}_s}$ as well as the execution times obtained from 10 different random distributions of measurements for each value of $N_{\mathbf{y}_s} = 10$. At this resolution, PICKLE is more accurate than MAP for most considered configurations and numbers of measurements. Tables 4a and 4b show results for unknown and known boundary conditions, respectively. Figure 6 shows the RF2 y field with the resolution $N_{VF} = 5900$ and the point errors in the PICKLE and MAP estimates of this y field obtained with $N_{\mathbf{y}_s} = 10, 25, 50,$ and 100 and unknown flux boundary conditions. It follows from Table 4 that the PICKLE ℓ_2 errors are smaller than those in MAP except the upper ranges of the errors for $N_{\mathbf{y}_s} = 10$ and 25 . The lower bound of ℓ_∞ errors is lower in the PICKLE method (except for $N_{\mathbf{y}_s} = 10$) while the upper bound is larger (except for $N_{\mathbf{y}_s} = 100$). The errors for unknown Neumann boundary conditions are slightly larger in both methods than those in the case with known Neumann boundary conditions.

Table 4: Performance of PICKLE and MAP for estimating the fine-resolution ($N_{FV} = 5900$) RF2 as functions of N_{y_s} with (a) unknown and (b) known Neumann boundary conditions.

(a) Unknown Neumann boundary conditions

		N_{y_s}			
solvers		100	50	25	10
least square iterations	PICKLE	9–11	11–15	11–16	14–35
	MAP	69–205	78–199	102–234	210–288
execution time (s)	PICKLE	206–265	196–217	188–203	208–290
	MAP	4072–8186	3977–10121	6031–12374	12459–16944
relative ℓ_2 error	GPR	0.103–0.162	0.219–0.395	0.349–0.503	0.458–0.846
	PICKLE	0.0211–0.0650	0.0560–0.150	0.0681–0.323	0.205–0.915
	MAP	0.119–0.140	0.157–0.188	0.179–0.247	0.211–0.336
absolute ℓ_∞ error	GPR	0.80–2.10	2.18–3.80	2.06–4.19	2.95–4.40
	PICKLE	0.348–0.834	0.476–2.04	0.715–2.32	1.70–4.19
	MAP	0.877–1.30	0.961–1.48	1.18–1.55	1.32–1.53

(b) Known Neumann boundary conditions

		N_{y_s}			
solvers		100	50	25	10
least square iterations	PICKLE	8–11	11–15	11–15	14–37
	MAP	86–129	84–136	69–128	65–109
execution time (s)	PICKLE	192–223	192–217	181–200	193–200
	MAP	4520–6330	4228–7124	6277–10348	6096–9333
relative ℓ_2 error	PICKLE	0.0193–0.0526	0.0497–0.145	0.0638–0.324	0.154–0.594
	MAP	0.104–0.128	0.121–0.168	0.150–0.211	0.179–0.308
absolute ℓ_∞ error	PICKLE	0.302–0.823	0.476–1.93	0.709–2.29	1.65–3.91
	MAP	0.922–1.37	0.900–1.62	1.06–1.69	1.41–1.71

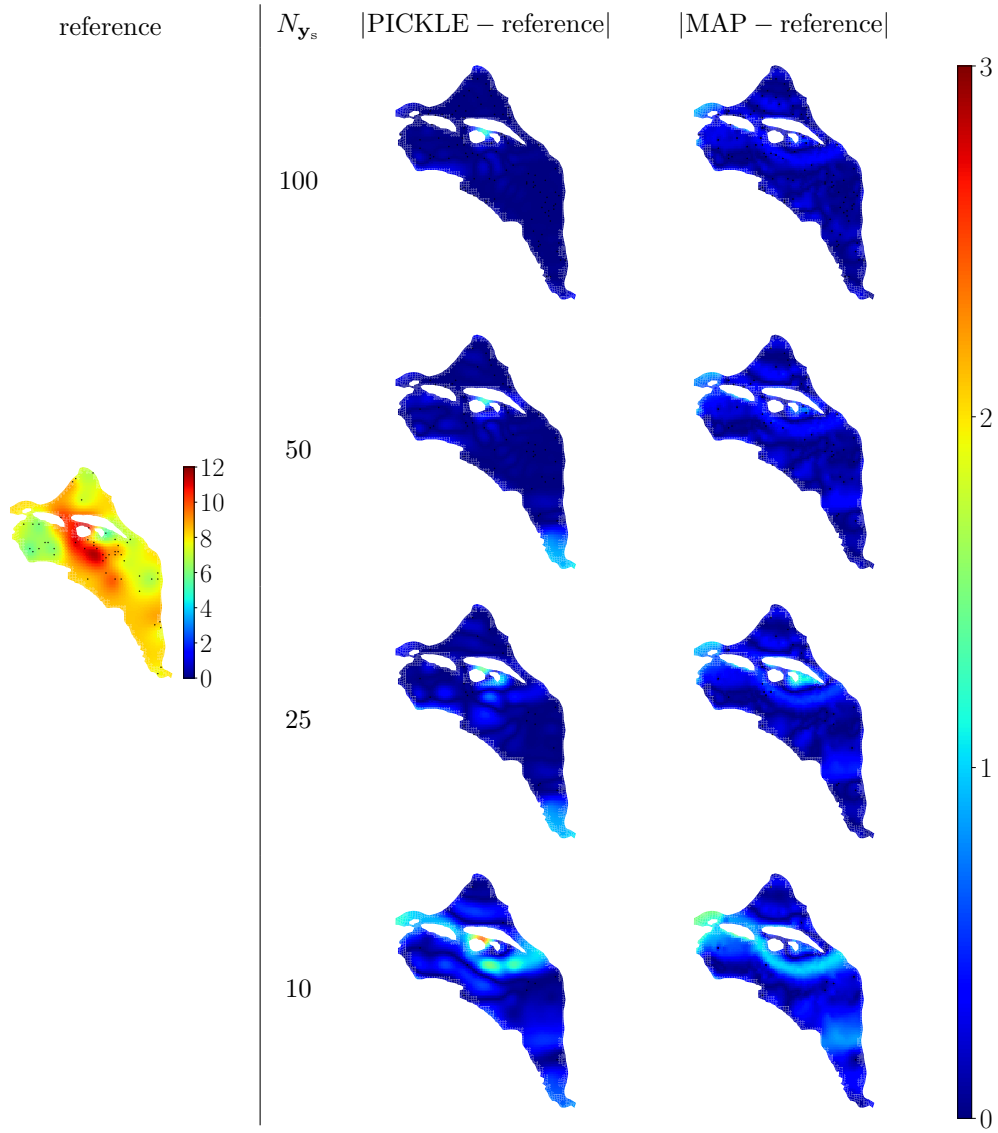


Figure 6: The fine-resolution ($N_{FV} = 5900$) RF2 reference y field and the point errors in the PICKLE and MAP estimates of the y field as functions of N_{y_s} given the unknown Neumann boundary conditions. The dots are the locations of the 100 observations of y .

4.4 Scaling of the execution time with the problem size

The comparison of Tables 3 and 4 shows that the execution times of both PICKLE and MAP increase with the mesh resolution; however, the execution time of PICKLE increases slower than that of MAP. To further study the dependence of the computational cost of PICKLE and MAP, in Figure 7 we plot the execution time of these methods as functions of N_{FV} for both the RF1 and RF2 reference fields. For these results, a mesh with $N_{FV} = 23600$ FV cells is generated by dividing each cell in the mesh with $N_{FV} = 5900$ in four. The number of y measurements in all simulations is set to $N_{y_s} = 100$. Figure 7 also shows the power-law model fits for both methods. We note that for $N_{FV} = 23600$, the MAP method did not converge after running for two days. Therefore, the power law relationships for the MAP method are obtained based on the execution times for $N_{FV} = 1475$ and 5900 and used to estimate MAP’s execution times for the highest resolution. From Figure 7, we see that the PICKLE and MAP execution times increase as $N_{FV}^{1.1}$ and $N_{FV}^{3.2}$, respectively, for both the RF1 and RF2 fields. The close to linear dependence of PICKLE’s execution time on the problem size gives it a computational advantage over the MAP method.

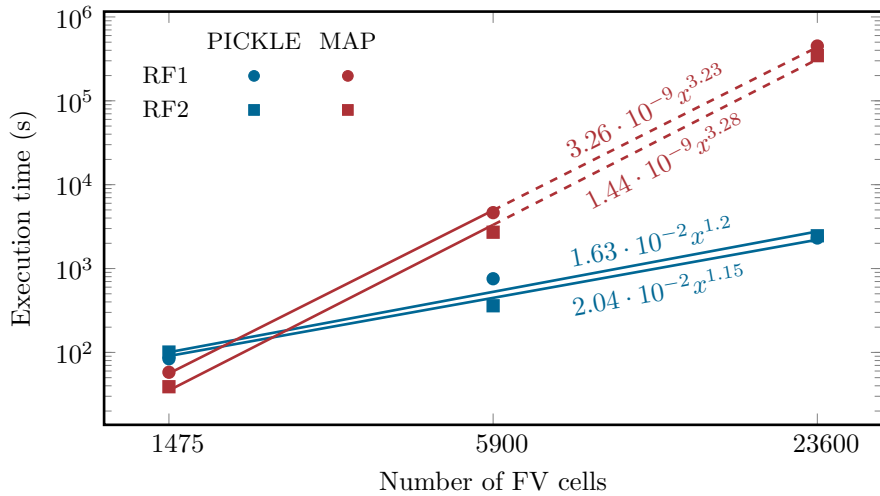


Figure 7: Execution times of PICKLE and MAP versus the number of FV cells for the RF1 and RF2 reference fields. The execution times of MAP for the mesh with 23600 FV cells are estimated by extrapolation.

4.5 Modeling u and y measurements corresponding to arbitrary boundary conditions

In many natural systems such as the Hanford Site, boundary conditions can change with time. Once “trained” for one value of the boundary conditions, PICKLE can be used without additional retraining to assimilate data corresponding to any boundary condition, i.e., $C_u(x', x'')$, that is calculated from the MC simulations for certain boundary conditions $(q_N^*(x), u_D^*(x))$ can be used to estimate y and u using measurements that correspond to any values of $(q_N(x), u_D(x))$. This is because for the deterministic (known) boundary conditions $(q_N(x), u_D(x))$, $C_u(x', x'')$ does not depend on the values of $(q_N(x), u_D(x))$. For stochastic boundary conditions, $C_u(x', x'')$ depends only on the covariances of $q_N(x)$ and $u_D(x)$ and not on their mean values.

As an example, we consider a case where the Dirichlet boundary condition $u_D(x)$ incrementally changes with time in the range $[u_D^{min}, u_D^{max}]$ in response to the changes in

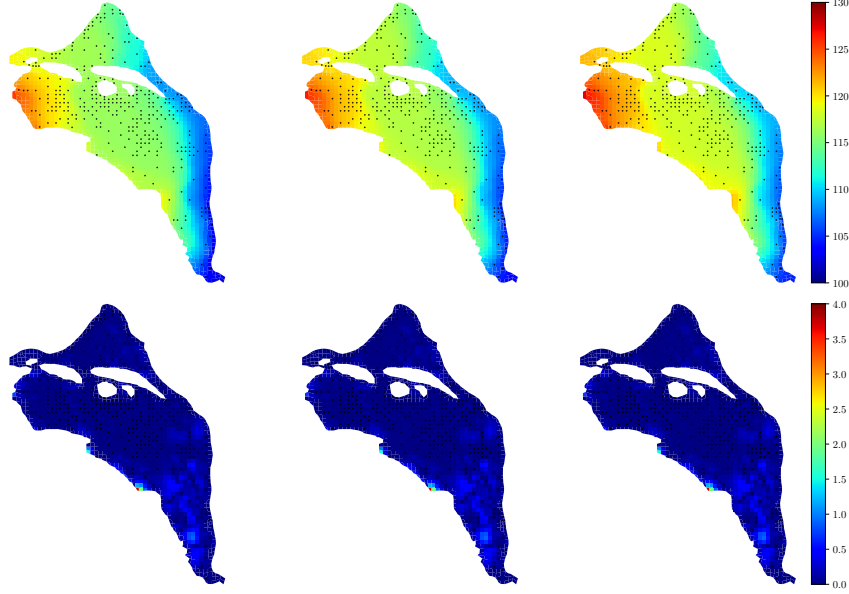


Figure 8: The PICKLE estimates $\hat{u}(i)$ ($i = 1, 2, 3$) (top row) and the point errors with respect to the reference fields $u(i)$ (bottom row). The dots are locations of the wells where u measurements are available.

the water level in the Columbia and Yakima Rivers. We denote $u_{\mathcal{D}}^{(i)}(x)$ ($i = 1, \dots, N_t$) as the Dirichlet BC at each of N_t time intervals. At the i th time interval, the \mathbf{u}_s^i measurements are collected at $N_{\mathbf{u}_s}$ spatial locations. The Neumann boundary conditions are assumed to be statistically known, i.e., the mean and covariance of $q_{\mathcal{N}}(x)$ are assumed to be known, and these statistical moments are assumed to be constant in time. The \mathbf{y}_s are available at $N_{\mathbf{y}_s}$ locations (\mathbf{y}_s do not change in time). To model \mathbf{y}_s and $\mathbf{u}_s^{(i)}$ data, the covariance function $C_u(x', x'')$ can be found from the MC method as described in Section 3.2 with $u_{\mathcal{D}}(x) = u_{\mathcal{D}}^*(x)$, where $u_{\mathcal{D}}^*(x)$ is any one BC from $\{u_{\mathcal{D}}^{(i)}\}_{i=1}^{N_t}$. We emphasize that $C_u(x', x'')$ should be computed only for one BC from $\{u_{\mathcal{D}}^{(i)}\}_{i=1}^{N_t}$ and then can be applied to any boundary condition from $\{u_{\mathcal{D}}^{(i)}\}_{i=1}^{N_t}$.

To apply PICKLE to the $\mathbf{u}_s^{(i)}$ measurements, in addition to $C_u(x', x'')$ we need to estimate $\bar{u}^{(i)}(x)$ that, unlike the covariance, depends on $u_{\mathcal{D}}^{(i)}$. Section 3.2 describes the MC method for computing $\bar{u}^{(i)}(x)$ that could be expensive to perform for each $u_{\mathcal{D}}^{(i)}$ ($i = 1, \dots, N_t$). Here, we propose to approximately compute the $\bar{u}^{(i)}(x)$ from the mean Darcy flow equation

$$\nabla \cdot [\bar{T}^c(x) \nabla \bar{u}^{(i)}(x)] = 0, \quad x \in D, \quad (21)$$

$$\bar{T}^c(x) \nabla \bar{u}^{(i)}(x) \cdot n(x) = -\bar{q}_{\mathcal{N}}(x), \quad x \in \Gamma_{\mathcal{N}}, \quad (22)$$

$$\bar{u}^{(i)}(x) = u_{\mathcal{D}}^{(i)}(x), \quad x \in \Gamma_{\mathcal{D}}, \quad (23)$$

where $\bar{T}^c = \exp(\bar{y}^c)$, and $\bar{y}^c(x)$ is given by Eq. (16). Eq. (22) is an approximation to the MC solution for $\bar{y}^c(x)$ that disregards the term $\nabla \cdot [T'(x) \nabla u^{(i)'}(x)]$, where $T'(x) = T^c(x) - \bar{T}^c(x)$ and $u^{(i)'}(x) = u^{(i)}(x) - \bar{u}^{(i)}(x)$.

To test the proposed approximate PICKLE model, we assume that the reference y field is given by the RF1 field from which we draw $N_{\mathbf{y}_s} = 100$ measurements of y at random locations. Furthermore, we assume that $u(x)$ is sampled at $N_{\mathbf{u}_s} = 323$

locations, and that three measurements of $u(x)$ are available at each location forming three vectors of u measurements $\mathbf{u}_s^{(i)}$ ($i = 1, 2, 3$). The corresponding boundary conditions $u_{\mathcal{D}}^{(i)}(x)$ ($i = 1, 2, 3$) are constructed as follows: $u_{\mathcal{D}}^{(2)}(x)$ is given by the calibration study (Cole et al., 2001), $u_{\mathcal{D}}^{(1)}(x) = u_{\mathcal{D}}^{(2)}(x) - 1\text{m}$, and $u_{\mathcal{D}}^{(3)}(x) = u_{\mathcal{D}}^{(2)}(x) + 1\text{m}$. Three reference fields $u^{(i)}(x)$ are computed by solving Eqs. (1)–(3) with $y(x)$ given by the RF1 y field and subject to the Dirichlet BCs $u_{\mathcal{D}}^i$ ($i = 1, 2, 3$). The vector \mathbf{u}_s^i is drawn from the reference field $u^{(i)}(x)$. We compute $C_u(x', x'')$ (and $\bar{u}^{(2)}$) from MCS for $u_{\mathcal{D}}(x) = u_{\mathcal{D}}^{(2)}(x)$. The mean u fields $\bar{u}^{(1)}$ and $\bar{u}^{(3)}$ are approximately computed from Eqs. (21)–(23). Figure 8 shows the PICKLE estimates $\hat{u}^{(i)}$ and the corresponding point errors with respect to the reference fields $u^{(i)}$ ($i = 1, 2, 3$). For all three fields, the errors in the estimated u fields are similar, with the average relative errors less than 0.5% and maximum point errors less than 4%. These results show that the PICKLE model trained for one boundary condition ($u_{\mathcal{D}}^{(2)}(x)$ in this case) can be used to accurately predict the u field for any boundary condition. Note that in general, the PICKLE estimate of y from the \mathbf{u}_s^i and \mathbf{y}_s measurements could be different because the parameter estimation is an ill-posed problem. However, for this test problem and the \mathbf{u}_s^i measurements, we find that the PICKLE estimates of y are within 0.01% of each other.

5 Discussion and Conclusions

We proposed the PICKLE method for assimilating data in models with unknown and time changing boundary conditions and used it to estimate the transmissivity and hydraulic head in the two-dimensional steady-state groundwater model of the Hanford Site with incrementally varying-in-time Dirichlet boundary conditions and uncertain Neumann boundary conditions. The PICKLE method is based on the approximation of unknown parameters and state variables with CKLEs. The CKLE approximation of a field enforces (exactly matches) the field measurements and the covariance structure, that is, it models the field as a realization of the conditional Gaussian field with a prescribed covariance function. To test the applicability of CKLE-based approximations for natural systems such as the Hanford Site, we considered two reference log transmissivity fields, both representing the complexity of the Hanford Site. The first transmissivity field, referred to as the RF1 field, is constructed by depth-averaging the conductivity field obtained in a previous calibration study that did not make any regularization Gaussianity assumptions. The RF2 reference (natural-log-)transmissivity field was constructed using the Gaussian process regression (or Kriging) based on 50 values of the RF1 (natural-log-)transmissivity field with locations randomly selected from the 323 locations of the wells at the Hanford Site. By construction, the RF2 field is smoother than the RF1 field. The comparison with the MAP method, a standard method for solving inverse problems, for RF1 and RF2 reference fields reveals the following relative advantages and disadvantages of the PICKLE method.

- For the synthetic data generated with RF1 and RF2 y fields, we demonstrated that the MAP and PICKLE execution times scale with the problem size as $N_{FV}^{1,15}$ and $N_{FV}^{3,27}$, respectively, where N_{FV} is the number of FV cells. The close to linear dependence of PICKLE’s execution time on the problem size gives PICKLE a computational advantage over the MAP method for large-scale problems. We consider this to be the main advantage of the PICKLE method.
- For the same number of measurements, the accuracy of PICKLE and MAP depends on the measurements locations. The MAP method is on average more accurate for the RF1 field, and the PICKLE method is more accurate for the RF2 field for most considered cases.
- The execution time of PICKLE and MAP increases and the accuracy decreases as the roughness of the parameter field increases.

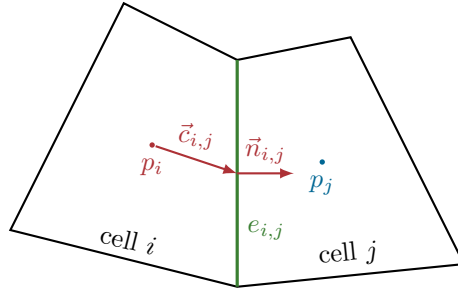


Figure A1: Two adjacent cells used to define the two-point finite-volume discretization model.

- In the PICKLE method, the execution time and accuracy increase with the increasing number of CKL terms. In this work, as a baseline we used $N_y = N_u = 1000$ that corresponds to $\text{rtol} < 10^{-6}$. We stipulate that this criterion is sufficient to obtain a convergent estimate of y with respect to the number of CKL terms.
- The training of the PICKLE model should be performed only for one value of the boundary conditions and does not need to be updated as the boundary conditions change, which significantly reduces its cost.
- The accuracy of the PICKLE method depends on the ability of the truncated CKLEs to accurately approximate $y(x)$ and $u(x)$, which requires a certain degree of smoothness of the considered fields. We demonstrated that for y and u fields that are representative of the Handford Site, the CKLE approximations of the fields lead to results that are comparable in accuracy to the MAP method. However, CKL can also be used to approximate fields exhibiting step-like changes (e.g., at the boundaries of different geological formations) using a logistic function as was shown in (A. Tartakovsky et al., 2020).
- In the PICKLE method, computing the covariance function of u from MCS can become a computational bottleneck for large-scale problems. Two points should be made in this regard: (1) PICKLE’s reported execution times in the scalability study (and everywhere else in this work) include the time to perform MCS and the execution time of MAP increases significantly faster than that of PICKLE; and (2) MCS can be replaced with more computationally efficient alternatives, including the multilevel MC method, generative physics-informed machine learning models, Polynomial Chaos and other surrogate models, and the moment equation method.

6 Acknowledgments

This research was partially supported by the U.S. Department of Energy (DOE) Advanced Scientific Computing (ASCR) program. Pacific Northwest National Laboratory is operated by Battelle for the DOE under Contract DE-AC05-76RL01830. The data and codes used in this paper are available at <https://github.com/yeungyh/pickle.git>.

Appendix A Finite Volume Discretization

Figure A1 shows two adjacent cells in the finite-volume discretization model with their centers labeled as p_i and p_j , respectively. In this model, we assume that the transmissivity is linear within each cell i and its average value T_i is at its center.

The edge shared by the two cells, $e_{i,j}$, has dimension $|e_{i,j}|$. The stiffness matrix \mathbf{A} in Eq. (4) is defined as

$$\mathbf{A}[i,j] = \begin{cases} \sum_k \mathcal{T}_{ik} & \text{if } i = j, \\ -\mathcal{T}_{ij} & \text{if } i \neq j, \end{cases} \quad (\text{A1})$$

where

$$\begin{aligned} \mathcal{T}_{ij} &= [\tau_{i,j}^{-1} + \tau_{j,i}^{-1}]^{-1}, \\ \tau_{i,j} &= T_i |e_{i,j}| \frac{\vec{c}_{i,j} \cdot \vec{n}_{i,j}}{|\vec{c}_{i,j}|^2}. \end{aligned}$$

and T_i is the transmissivity in cell i . The right-hand side \mathbf{b} describes the boundary conditions, and is defined as

$$\mathbf{b}[i] = \begin{cases} \tau_{i,\Gamma} \mathbf{u}_{\mathcal{D}}[i] & i \in \Gamma_{\mathcal{D}}, \\ \mathbf{q}_{\mathcal{N}}[i] & i \in \Gamma_{\mathcal{N}}, \\ 0 & \text{otherwise,} \end{cases} \quad (\text{A2})$$

where $\tau_{i,\Gamma}$ is the transmissivity between cell i and the boundary.

Appendix B Computing MAP estimates

In this work, we compute MAP estimates by recasting the PDE-constrained optimization problem of Eq. (5) into an unconstrained nonlinear least-squares problem. Specifically, we aim to solve the problem

$$\min_{\mathbf{p}} \frac{1}{2} \|\mathbf{f}(\mathbf{p})\|_2^2, \quad (\text{B1})$$

with cost vector given by

$$\mathbf{f}(\mathbf{p}) = \begin{bmatrix} \mathbf{u}_s - \mathbf{H}_u \mathbf{u}(\mathbf{y}, \mathbf{q}) \\ \mathbf{y}_s - \mathbf{H}_y \mathbf{y} \\ \sqrt{\gamma} \mathbf{D} \mathbf{y} \\ \sqrt{\gamma} \mathbf{q} \end{bmatrix}, \quad \mathbf{p} = \begin{bmatrix} \mathbf{y} \\ \mathbf{q} \end{bmatrix}, \quad (\text{B2})$$

where \mathbf{H}_u and \mathbf{H}_y are the observation matrices in Eq (5).

Note that in Eq. (B1), we fold the PDE constraint into the cost function by treating \mathbf{u} explicitly as a function of the parameters \mathbf{p} .

For the least-square minimization problem, it is necessary to compute the Jacobian matrix of the cost vector with respect to the parameters \mathbf{p} , which is given by

$$\mathbf{J}(\mathbf{p}) = \frac{\partial \mathbf{f}(\mathbf{p})}{\partial \mathbf{p}} = \begin{bmatrix} -\mathbf{H}_u \partial \mathbf{u}(\mathbf{y}, \mathbf{q}) / \partial \mathbf{y} & -\mathbf{H}_u \partial \mathbf{u}(\mathbf{y}, \mathbf{q}) / \partial \mathbf{q} \\ -\mathbf{H}_y & 0 \\ \sqrt{\gamma} \mathbf{D} & 0 \\ 0 & \sqrt{\gamma} \mathbf{I} \end{bmatrix}. \quad (\text{B3})$$

It can be seen that the first block row of Eq. (B3) corresponds to the Jacobian of \mathbf{u} with respect to the parameters \mathbf{p} , for which we derive a formula as follows. Differentiating Eq. (4) with respect to the i th component of \mathbf{p} , we obtain

$$\frac{\partial \mathbf{l}}{\partial p_i} + \frac{\partial \mathbf{l}}{\partial \mathbf{u}} \frac{\partial \mathbf{u}}{\partial p_i} = \frac{\partial \mathbf{A}}{\partial p_i} - \frac{\partial \mathbf{b}}{\partial p_i} + \mathbf{A} \frac{\partial \mathbf{u}}{\partial p_i} = 0,$$

therefore,

$$\frac{\partial \mathbf{u}}{\partial p_i} = -\mathbf{A}^{-1} \left[\frac{\partial \mathbf{A}}{\partial p_i} - \frac{\partial \mathbf{b}}{\partial p_i} \right]. \quad (\text{B4})$$

Appendix C Solver Optimization

We implemented our solvers for both PICKLE and MAP in Python. In both solvers, TPFA is used as a finite volume model for the forward problem. Although we did not parallelize the solvers used in this paper, we optimized the codes in several ways as follows.

C1 Precomputing matrices

Because the properties of each cell, the observation locations of \mathbf{u}_s , \mathbf{y}_s , and the topology of the cell connections are fixed, the structures of the matrices also remain unchanged throughout the least-squares minimization of Eqs. (5) and (14). Thus, the matrices representing these fixed properties including the observation matrices \mathbf{H}_u , \mathbf{H}_y , and the regularization matrix \mathbf{D} can be precomputed in advance. For the stiffness matrix \mathbf{A} in Eq. (4) and the partial derivatives in the first block row of Eq. (B3), although their values change over each minimization iteration, their structures (the positions of nonzero components of the matrices) remain the same, and can be identified in advance. In addition, when the boundary conditions are known and constant in time, the aggregated contribution of the prescribed hydraulic head u_D and normal flux q_N to each FV cell i — $\mathbf{u}_D[i]$ and $\mathbf{q}_N[i]$ in Eq. (A2)—can also be precomputed. For MAP, the second to the fourth block rows and \mathbf{H}_u in the first block row of the Jacobian in Eq. (B3) are also constant throughout minimization because they only depend on the topology of the mesh. Therefore, these elements can also be precomputed ahead of time.

C2 Sparsity

Sparsity is maintained throughout the evaluations of the objective functions of both PICKLE and MAP, including the residual $\mathbf{l}(\mathbf{u}, \mathbf{y}, \mathbf{q})$ in Eq. (4), as well as their corresponding Jacobian matrices. This significantly reduces the storage and computation overhead because the increase in the resolution of the mesh quadruples the size of the matrices. However, the SciPy implementation of the sparse linear solver (`spsolve`) does not support sparse right-hand-side vectors and matrices. Furthermore, partial solvers that only compute solutions at measurement locations and do not have the ability to reuse sparse structural reordering are not supported by the package. Future optimization using these techniques would further reduce the execution times of both the MAP and PICKLE methods.

References

- Barajas-Solano, D., & Tartakovsky, A. (2019). Approximate Bayesian model inversion for PDEs with heterogeneous and state-dependent coefficients. *Journal of Computational Physics*, *395*, 247 - 262.
- Barajas-Solano, D. A., Wohlberg, B. E., Vesselinov, V. V., & Tartakovsky, D. M. (2014). Linear functional minimization for inverse modeling. *Water Resour. Res.*, *51*, 4516-4531. doi: 10.1002/2014WR016179
- Branch, M. A., Coleman, T. F., & Li, Y. (1999). A subspace, interior, and conjugate gradient method for large-scale bound-constrained minimization problems. *SIAM Journal on Scientific Computing*, *21*(1), 1-23. doi: 10.1137/S1064827595289108
- Chen, Y., Wiesel, A., & Hero, A. O. (2009, April). Shrinkage estimation of high dimensional covariance matrices. In *2009 IEEE International Conference on Acoustics, Speech and Signal Processing* (p. 2937-2940). doi: 10.1109/ICASSP.2009.4960239
- Cole, C. R., Bergeron, M. P., Wurstner, S. K., Thorne, P. D., Orr, S., & Mckinley, M. I. (2001). *Transient inverse calibration of Hanford site-wide groundwater model to Hanford operational impacts-1943 to 1996* (Tech. Rep.). Richland, Washington,

- United States: Pacific Northwest National Laboratory (PNNL).
- Giles, M. B. (2015). Multilevel monte carlo methods. *Acta Numerica*, *24*, 259–328. doi: 10.1017/S096249291500001X
- Herckenrath, D., Langevin, C. D., & Doherty, J. (2011). Predictive uncertainty analysis of a saltwater intrusion model using null-space monte carlo. *Water Resources Research*, *47*(5).
- Jarman, K. D., & Tartakovsky, A. M. (2013). A comparison of closures for stochastic advection-diffusion equations. *SIAM/ASA Journal on Uncertainty Quantification*, *1*(1), 319-347. doi: 10.1137/120897419
- Kitanidis, P. K. (1996). On the geostatistical approach to the inverse problem. *Advances in Water Resources*, *19*(6), 333–342.
- Li, J., & Tartakovsky, A. M. (2020). Gaussian process regression and conditional polynomial chaos for parameter estimation. *Journal of Computational Physics*, 109520.
- Lin, G., & Tartakovsky, A. M. (2010). Numerical studies of three-dimensional stochastic Darcy’s equation and stochastic advection-diffusion-dispersion equation. *Journal of Scientific Computing*, *43*(1), 92-117.
- Matheron, G. (1963). Principles of geostatistics. *Economic geology*, *58*(8), 1246–1266.
- Neuman, S. P. (1993). Eulerian-Lagrangian theory of transport in space-time non-stationary velocity fields: Exact nonlocal formalism by conditional moments and weak approximation. *Water Resources Research*, *29*(3), 633–645.
- Neuman, S. P., & Tartakovsky, D. M. (2009). Perspective on theories of non-fickian transport in heterogeneous media. *Advances in Water Resources*, *32*(5), 670–680.
- Picard, R. R., & Cook, R. D. (1984). Cross-validation of regression models. *Journal of the American Statistical Association*, *79*(387), 575–583.
- Rasmussen, C. E. (2003). Gaussian processes in machine learning. In *Summer school on machine learning* (pp. 63–71).
- Tartakovsky, A., Barajas-Solano, D., & He, Q. (2020). Physics-informed machine learning with conditional Karhunen-Loève expansions. *Journal of Computational Physics*, 109904.
- Tartakovsky, D. M., Lu, Z., Guadagnini, A., & Tartakovsky, A. M. (2003). Unsaturated flow in heterogeneous soils with spatially distributed uncertain hydraulic parameters. *Journal of Hydrology*, *275*(3-4), 182-193.
- Tipireddy, R., Barajas-Solano, D. A., & Tartakovsky, A. M. (2020a). Conditional Karhunen-Loève expansion for uncertainty quantification and active learning in partial differential equation models. *Journal of Computational Physics*, *418*, 109604.
- Tipireddy, R., Barajas-Solano, D. A., & Tartakovsky, A. M. (2020b). Conditional Karhunen-Loève expansion for uncertainty quantification and active learning in partial differential equation models. *Journal of Computational Physics*, *418*, 109604. Retrieved from <http://www.sciencedirect.com/science/article/pii/S0021999120303788> doi: <https://doi.org/10.1016/j.jcp.2020.109604>
- Yang, L., Treichler, S., Kurth, T., Fischer, K., Barajas-Solano, D., Romero, J., ... others (2019). Highly-scalable, physics-informed GANs for learning solutions of stochastic PDEs. In *2019 IEEE/ACM Third Workshop on Deep Learning on Supercomputers (DLS)* (pp. 1–11).
- Yang, X., Barajas-Solano, D., Tartakovsky, G., & Tartakovsky, A. M. (2019). Physics-informed coKriging: A Gaussian-process-regression-based multifidelity method for data-model convergence. *Journal of Computational Physics*, *395*, 410 - 431.
- Yang, X., Li, W., & Tartakovsky, A. (2018). Sliced-inverse-regression-aided rotated compressive sensing method for uncertainty quantification. *SIAM/ASA Journal on Uncertainty Quantification*, *6*(4), 1532-1554.

- Yang, X., Tartakovsky, G., & Tartakovsky, A. (2018). Physics-informed kriging: A physics-informed gaussian process regression method for data-model convergence. *arXiv preprint arXiv:1809.03461*.
- Yoon, H., Hart, D. B., & McKenna, S. A. (2013). Parameter estimation and predictive uncertainty in stochastic inverse modeling of groundwater flow: Comparing null-space monte carlo and multiple starting point methods. *Water Resources Research*, 49(1), 536-553.